Strain localization and fatigue crack formation at (0001) twist boundaries in titanium alloys

S. Hémery, J.C. Stinville, F. Wang, M.A. Charpagne, M.G. Emigh, T.M. Pollock, Valery Valle

To cite this version:

S. Hémery, J.C. Stinville, F. Wang, M.A. Charpagne, M.G. Emigh, et al.. Strain localization and fatigue crack formation at (0001) twist boundaries in titanium alloys. Acta Materialia, 2021, 219, pp.117227. ⟨10.1016/j.actamat.2021.117227⟩. ⟨hal-03681156⟩

Strain Localization and Fatigue Crack Formation at (0001) Twist Boundaries in Titanium Alloys

S. Hémery[a], J.C. Stinville[b,*], F. Wang[b], M.A. Charpagne[b], M. Emigh[b], T.M. Pollock[b], V. Valle[a]

[a] Institut Pprime, ISAE-ENSMA, Université de Poitiers, CNRS UPR 3346, Téléport 2, 1 avenue Clément Ader, BP 40109, Futuroscope-Chasseneuil Cedex, 86961, France

[b] Materials Department, University of California Santa Barbara, Santa Barbara, CA, 93106, USA

[*] Now at Departments of Materials Science and Engineering, University of Illinois at Urbana-Champaign, Urbana, IL, USA

Abstract

The process of crack initiation has been investigated in three widely used titanium alloys with different microstructures and loading conditions. Using low-cycle fatigue tests, a unique crack nucleation mechanism involving strain localization at (0001) twist boundaries has been identified. In order to constitute a potential crack initiation site, the twist boundary must experience a high resolved shear stress and a high normal stress. Crack initiation is also more likely to occur at these boundaries for twist angles in the 10° - 20° range. Deformation prior to crack initiation at these rare microstructural configurations has been characterized using transmission electron microscopy and high-resolution digital image correlation across large fields of view. The (0001) twist boundaries are preferential locations for early and intense strain localization. Prior to crack nucleation, deformation proceeds via shear along such boundaries where no β layer at the interface was evidenced. The presently discussed crack formation mechanism is believed to be of broad relevance as it is not significantly influenced by microstructural parameters such as the α grain size, the degree of microtexture, the β phase fraction or the surrounding microstructure as well as α and β compositions.

Keywords:

Titanium alloys, slip, grain boundary, fatigue crack initiation, strain localization.

Graphical abstract:

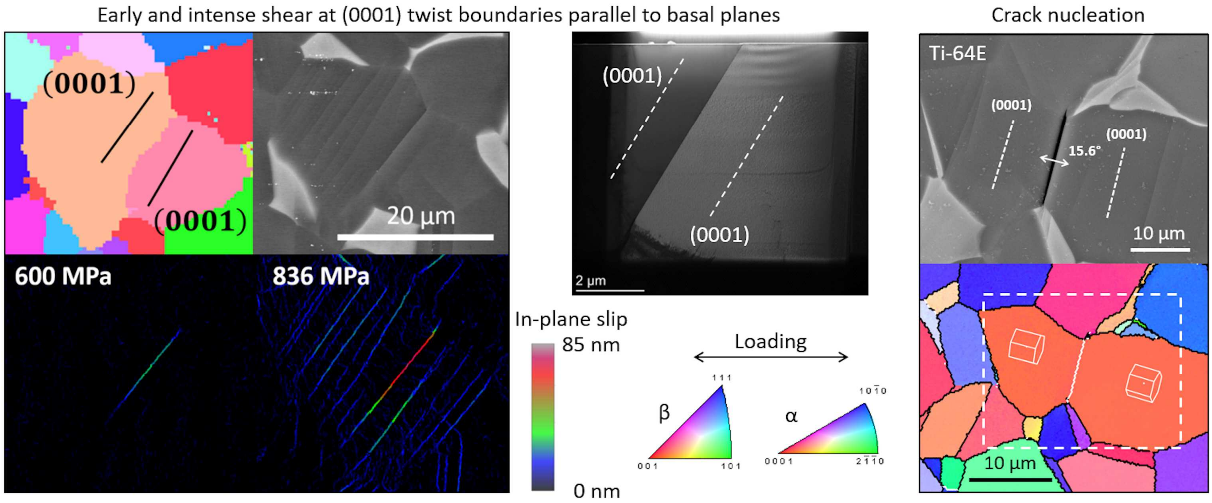

1. Introduction

Recent failures of aircraft components have highlighted that important gaps remain in the understanding and the prediction of the behavior of titanium alloys subjected to cyclic loading [1]. While the cold dwell-fatigue issue [2–5] and the detrimental consequences of microtextured regions [6–9] were identified as key features, limited lifetime prediction capabilities are also brought to light. The recent development of microstructure sensitive simulation approaches offers promising insights into improved lifetime assessment [10,11] as the specificities of local microstructural heterogeneities result in a substantial fatigue-life variability [12–14]. However, these prediction capabilities rely on the determination of fatigue indicator parameters that account for experimentally identified physical processes such as driving crack initiation [15,16].

Despite numerous studies focused on fatigue crack formation mechanisms over several decades, the relation between fatigue crack nucleation and microstructure remains unclear [17]. This situation partly pertains to the variety of titanium alloy compositions and microstructures obtained through different thermo-mechanical processing routes [18–20] as well as employed testing conditions. For instance, whether cracks nucleate in primary α [14,21–24] or transformed β regions [25,26] is under debate in bi-modal microstructures [18]. This results notably from elemental partitioning between primary and secondary α regions [25]. In contrast, it is quite widely accepted that initiation facet formation results from slip activity. While basal slip is generally considered as a preliminary step for fatigue crack formation in different α+β alloys [14,21,27], it is worth noting that cracks have been more rarely observed to nucleate on prismatic slip bands [22,28,29]. Specificities of basal slip have been investigated using monotonic loadings in prior studies. As compared to prismatic slip, basal slip is activated at lower applied stresses [30,31], induces a higher plastic strain [32], generates intense strain localization [33] and exhibits a higher strain rate sensitivity [34]. A high Schmid factor and a low misorientation between the c-axis of the hexagonal close-packed (HCP) lattice and the loading direction are two important features that favor crack nucleation. It reveals that a high resolved shear stress for incipient slip and a high normal stress for crack opening are required to promote crack nucleation [5,21]. Analysis of crystallographic orientations also revealed that a high stress normal to the nucleated crack is promoted by the high stiffness along the (0001) direction [21,35]. Joseph et al. [17] suggested the occurrence of a double-end pile up mechanism as originally introduced by Tanaka and Mura [36] as the root cause for crack formation on the basal plane. More recently, it has been shown that cracks form at (0001) twist boundaries where intense slip was localized in Ti-6Al-4V subjected to low-cycle fatigue and dwell-fatigue loadings [37]. However, the crack formation process, the relevance for other alloys and microstructures, and whether the first cracks are located at these microstructural configurations are not completely clear yet.

Alternative crack nucleation scenarios based on facet formation resulting from incoming slip have been proposed. Pioneering work by Neal and Blenkinshop has suggested that facets form by cleavage on a $\{10\bar{1}7\}$ plane due to restricted prismatic slip in the same α grain [24]. This mechanism accounts for experimental observations of near-basal cracking through a possible role of hydrogen since the $\{10\bar{1}7\}$ plane is a known hydride plane in Ti-Al alloys [38]. The generation of strain incompatibilities and stress concentrations required for crack formation largely pertain to the plastic anisotropy of HCP α Ti. This is also illustrated by the observation of crack initiation sites at the interface between highly misoriented microtextured regions [39]. A similar rationale was held to explain dwell-fatigue crack initiation which involves microstructural configurations composed of a grain suitably oriented for basal or prismatic slip activation ("soft" grain) adjacent to a grain unsuitably oriented for slip ("hard" grain) [2]. Piled-up dislocations induce a stress concentration in the neighboring "hard" grain, which triggers basal or near basal facet nucleation. Increased stress magnitudes in the "hard" grain can result from stress redistribution due to cold creep under sustained loads such as encountered during dwell-fatigue tests and induce a life debit as compared to conventional fatigue tests [3,40,41]. This mechanism, widely accepted for dwell-fatigue, is sometimes also considered for conventional fatigue [4,42].

In the present article, we aim at obtaining an improved understanding of crack formation processes and associated variations in different titanium alloys with various microstructures through usage of similar testing conditions and characterization procedures. Three industrially relevant near-α and α+β titanium alloys (Ti-6Al-4V, Ti-6Al-2Sn-4Zr-2Mo and Ti-6Al-2Sn-4Zr-6Mo) with bi-modal and equiaxed microstructures were tested in the low-cycle fatigue regime until a few nucleated cracks were detected. The existence of a unique mechanism is assessed based on scanning electron microscopy (SEM) and electron back-scattered diffraction (EBSD) characterization of the microstructure surrounding the cracks. Deformation at these critical microstructural configurations was then investigated using in-situ SEM high-resolution digital image correlation (HR-DIC) measurements and site specific transmission electron microscopy (TEM) characterization. A fundamental understanding of the complete process from incipient plasticity to crack formation in Ti alloys is finally provided.

2. Materials and experiments

2.1 Alloys and microstructures

Ti-6Al-2Sn-4Zr-2Mo (Ti-6242) and Ti-6Al-2Sn-4Zr-6Mo (Ti-6246) alloys provided by Timet were investigated in the present study. The microstructure results from processing in the α+β field followed by an annealing at 750 °C. A final ageing treatment of 8 h at 593 °C was applied. Ti-6242 and Ti-6426 exhibit triplex microstructures composed of equiaxed α and bi-lamellar α within the residual β matrix. In addition, Ti-6Al-4V (Ti-64) was considered with three different microstructures. Ti-64 with ultra-fine grain structure provided by the US Air Force Research Laboratory was heat treated to obtain an equiaxed (E) microstructure (Ti-64E) with a low degree of microtexture. For this purpose, annealing at 950 °C for 2 h followed by cooling at a rate of 6 °C per hour was applied before a 2 h final treatment at 700 °C. Commercially available mill-annealed Ti-64 rolled plate fabricated by Timet was heat treated at 926 °C for 4 h and cooled to room temperate at 18 °C per hour. The resulting equiaxed microstructure exhibits a high degree of microtexture (MTR) [7]. This material is denoted as Ti-64MTR in the following. Finally, Ti-6Al-4V with a bi-modal (BM) microstructure (Ti-64BM) was provided by Safran Aircraft Engines. The duplex microstructure of Ti-64BM is composed of primary α grains and transformed β regions where lamellar α is embedded in residual β phase. The measured compositions of the alloys used in the present study are given in table 1. The microstructures of the investigated alloys are presented in figure 1a. Microstructural features including α grain sizes and area fractions as well as average lamella thicknesses are given in table 2. Examination of the micrographs shown in figure 1a shows significantly different retained β fractions. Typical β phase fractions reported in the literature for the studied alloys range from ≈ 10 % for Ti-6242 [43] to ≈ 30 % for Ti-6246 [44]. Ti-64 has an intermediate β fraction [44,45]. Crystallographic orientation maps showing the degree of microtexture in the different materials are presented in figure 1b. The tensile properties were assessed with a strain rate of 10^{-2} s^{-1}, which was chosen to mimic the loading rate used for cyclic tests. The engineering stress – strain curves are reported in figure 1c. The Young's modulus, the yield strength, the ultimate tensile strength and the elongation are given in table 3 for all materials.

Alloy	Al	V	Sn	Zr	Mo	Si	Fe	O
Ti-6242	6.08	-	2.00	4.03	1.99	0.074	0.02	0.11
Ti-64BM	6.52	4.22	-	-	-	-	0.14	0.21
Ti-64E	6.3	4.1	-	-	-	-	0.18	0.18
Ti-64MTR	6.28	4.09	-	-	-	-	< 0.19	0.18
Ti-6246	6.20	-	2.01	4.10	6.00	0.05	0.08	0.10

Table 1: Composition of the alloys used in this work in weight % (Ti is balance).

Alloy	Primary α grain size (μm)	Primary α area fraction (%)	Lamella thickness (μm)	Nano-lamella thickness (μm)
Ti-6242	11	65	0.8	0.04
Ti-64BM	14	40	0.5	-
Ti-64E	9	-	-	-
Ti-64MTR	3.4	-	-	-
Ti-6246	6	57	0.6	0.04

Table 2: Microstructural features of the materials used in this work

Alloy	Young's modulus (GPa)	Yield strength (MPa)	Ultimate tensile strength (MPa)	Elongation (%)
Ti-6242	118	966	1013	13.7

Ti-64BM	118	998	1042	15.2
Ti-64E	112	919	938	18.6
Ti-64MTR	104	993	1023	13.4
Ti-6246	114	1057	1107	12.8

Table 3: Tensile properties with a strain rate of 10^{-2} s^{-1}

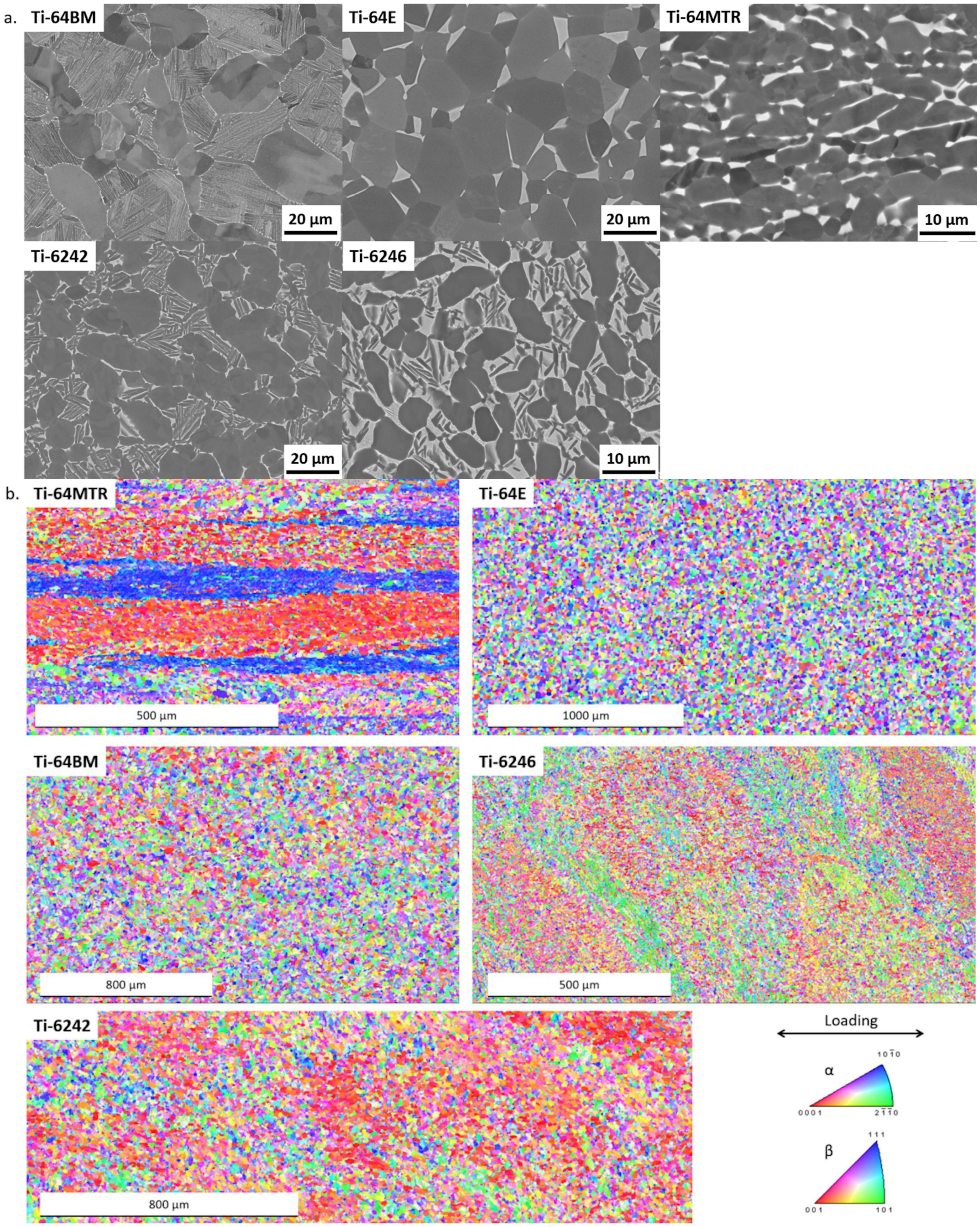

c.

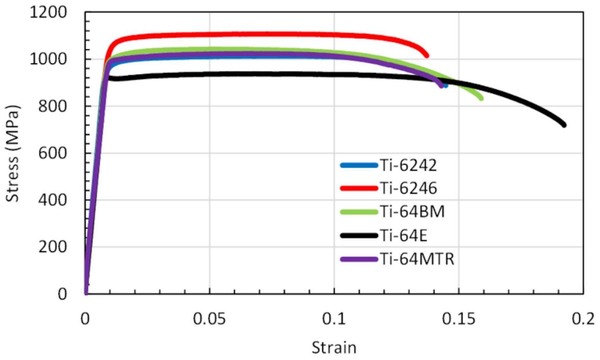

Figure 1: a. Backscattered electron micrographs showing the microstructures of Ti-6242, Ti-64BM, Ti-6426, Ti-64MTR and Ti-64E, b. Crystallographic orientations along the loading direction (horizontal) showing the degree of microtexture in Ti-6242, Ti-64BM, Ti-6426, Ti-64MTR and Ti-64E and c. Engineering stress – strain curves showing the tensile behaviors of Ti-6242, Ti-64BM, Ti-6426, Ti-64MTR and Ti-64E

2.2 Fatigue testing

Dogbone shaped specimens with a gage length of 10 mm, a gage width of 2 mm and a thickness about 0.8 mm were machined using electrical discharge machining. The squared cross section and the area in the gage length of the specimens are very suitable for SEM detection of small cracks as carried out in this study, while considering a representative microstructural area. Crack nucleation occurred randomly over the whole gage length, indicating a negligible influence of stress concentrations at edges. Both faces were ground finished with 4000 grit SiC paper. A polishing step is then applied on one face using a 9 µm diamond suspension before a final polishing using a mixture of 90 % suspension containing 0.04 µm silica particles and 10 % H_2O_2.

The specimens were tested at room temperature using an Instron 8862 universal testing machine. A load ratio of 0.1 was applied, leading to a positive mean stress. Loading was achieved in 1 s. The peak stress (σ_{max}) was held for 1 s. The specimen was unloaded in 1 s and the minimum stress (σ_{min}) was held for 1 s. The loading waveform is shown schematically in figure 2a. The strain is derived using an extensometer. Tests were carried out with peak stress values in the 85 % - 95 % of the yield strength range. The tests were stopped before failure of the specimen. The cumulated plastic strain is plotted in figure 2b as a function of the number of cycles for the different titanium alloys.

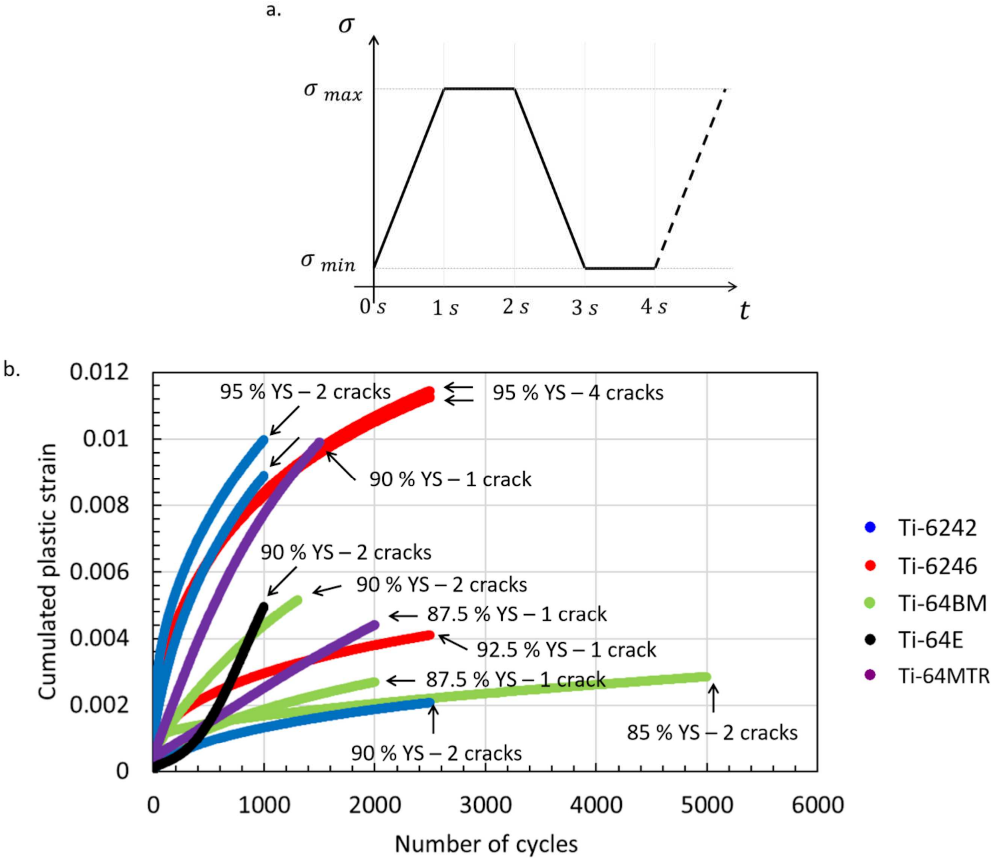

Figure 2: a. Applied loading waveform, b. Cumulated plastic strain as a function of the number of cycles. The number of detected nucleated cracks and the applied peak stress as a fraction of the yield strength (YS) are indicated.

2.3 Microstructure characterization techniques

After mechanical testing, the whole gage length of the specimen (20 mm²) was characterized using a TESCAN VEGA 3 SEM to detect nucleated cracks. Approximately 200 back-scattered electron micrographs are taken with a x800 magnification using an automated routine in order to map the gage length of each specimen. The number of cracks identified for each test is indicated in figure 2b for the different investigated titanium alloys. With this approach, cracks as small as a few microns could be successfully detected. It is noteworthy that such cracks could not be distinguished from slip bands using optical microscopy. Once identified, the cracks and the surrounding microstructure were observed at higher magnifications using a JEOL 7000F SEM. In addition, the local crystallographic orientations were characterized using the EBSD technique. A JEOL 6100 SEM equipped with a Hikari detector manufactured by EDAX was employed for that purpose. Diffraction patterns were acquired using an accelerating voltage of 25 kV, a 5 × 5 binning (128 x 96 pixels) and a beam current of 3 nA. A 0.2 μm step was applied. EBSD data was processed using the TSL OIM Analysis software. Grain boundaries with [0001] misorientations were identified using a 5° threshold on the misorientation between c-axes. A few crack initiation sites were chosen for a detailed characterization of the microstructure underneath the specimen surface. Thin foils were extracted using a Helios NanoLab G3 CX focused ion beam (FIB) and the microstructure surrounding the crack was then observed in transmission (TSEM) using a Scanning Transmission Electron Microscopy (STEM) detector.

Additional TEM analyses were carried out on targeted regions in a pre-deformed specimen. FIB lift-out samples were extracted using a ThermoFisher Helios by conventional FIB milling at 30 kV and with typical probe current of 2.5 nA. FIB thinning was performed, consisting of cleaning cross-sections with near edge-on focused beam. This cleaning cross-section was repeated from 30 kV with decreasing probe current from 0.28 nA to 93 pA, then at 16 kV and a probe current of 45 pA, and finally at 5 kV and 16 pA to minimize introduction of defects by FIB. After FIB cleaning, electron transparent specimens with thicknesses of approximately 100 nm are obtained. Scanning transmission electron microscopy (STEM) and high resolution scanning transmission electron microscopy (HRSTEM) analyses were carried out on a ThermoFischer Talos microscope under an accelerating voltage of 200 kV and equipped with a Super-X EDS detector system. Data was acquired with the Velox software. The presented high angle annular dark field (HAADF) - STEM micrographs were obtained after drift corrected frame integration, also performed in Velox.

2.4 In situ tensile testing and high-resolution digital image correlation

An in-situ tensile test was performed using a custom in-situ ± 5000 N stage within a ThermoFisher Versa3D microscope with field-emission gun on Ti-64E flat dogbone shaped specimens with a gauge section of 1 × 3 mm^2 and a length of 14 mm. The tensile test was performed at a strain rate of about 10^{-5} s^{-1} and interrupted at stress levels ranging from 600 MPa to 836 MPa. The total test duration was approximately 26 hours. Macroscopic strain was measured in-situ using strain gauge and fiducial markers located at both ends of the gauge length. Prior to testing, the specimen was polished with SiC papers up to 1200 grit, followed by polishing with a 3 μm diamond suspension and then chemomechanical polishing with 0.05 μm colloidal silica for 12 hours. A speckle pattern consisting of gold nanoparticles with average particle size of 60 nm was deposited on the surface for HR-DIC measurements, following the procedure developed by Kammers et al. [46]. Microstructure characterization was performed by EBSD measurements with an EDAX OIM-Hikari XM4 EBSD detector using a step size of 0.4 μm. Diffraction patterns were acquired using an accelerating voltage of 30 kV, a 4×4 binning and a beam current of 0.2 nA. SEM images sets were acquired for HR-DIC before loading and under load following the guidelines of Kammers and Daly [46] and Stinville et al. [47]. A National Instruments™ scan controller and acquisition system (DAQ) were used to control beam scanning in the ThermoFisher microscope. This custom beam scanner removes the SEM beam defects associated with some microscope scan generators [47]. Tiles of 12 × 6 images before and after deformation with an image overlap of 15% were used to map regions of interest. DIC calculations were performed on these series of images and results were merged using a pixel resolution merging procedure. Additional details on the experimental procedure are given elsewhere [48]. Two regions of 1 × 0.5 mm^2 were investigated. Typical subset sizes of 31×31 pixels (696 nm×696 nm) with a step size of 3 pixels (67 nm) were used for DIC. DIC was performed using the Heaviside-DIC method [49,50]. The sample preparation, imaging conditions and Heaviside-DIC parameters allow for a discontinuity detection resolution of about 10 nm [49,50]. The resulting data consists of maps of the location and amplitude of the slip events at a given loading step. The in-plane slip displacement, provided in nanometers, corresponds to the physical in-plane shearing induced by each single slip event at the surface of the specimen during deformation [49]. The in-plane slip direction was also derived from the data and compared with the projection of the Burgers vectors onto the surface [49]. Examples of in-plane slip displacement maps after deformation are provided in figure 3, alongside with the reconstructed stress – strain curve, showing that DIC data was collected at macroscopic stresses of 600 MPa, 700 MPa, 800 MPa and 836 MPa. The associated EBSD map and BSE image after deformation at 836 MPa are reported as well. For the sake of visualization, the HR-DIC maps are displayed in the present article using a "maximum" filter with a radius of 4 pixels that artificially increases the thickness of the slip event on the in-plane slip amplitude maps. The axial loading direction is horizontal in all maps. Data registration between EBSD and HR-DIC maps was done using a large number of pairs of control points that serve to compute the distortion function between EBSD and DIC data as detailed elsewhere [51].

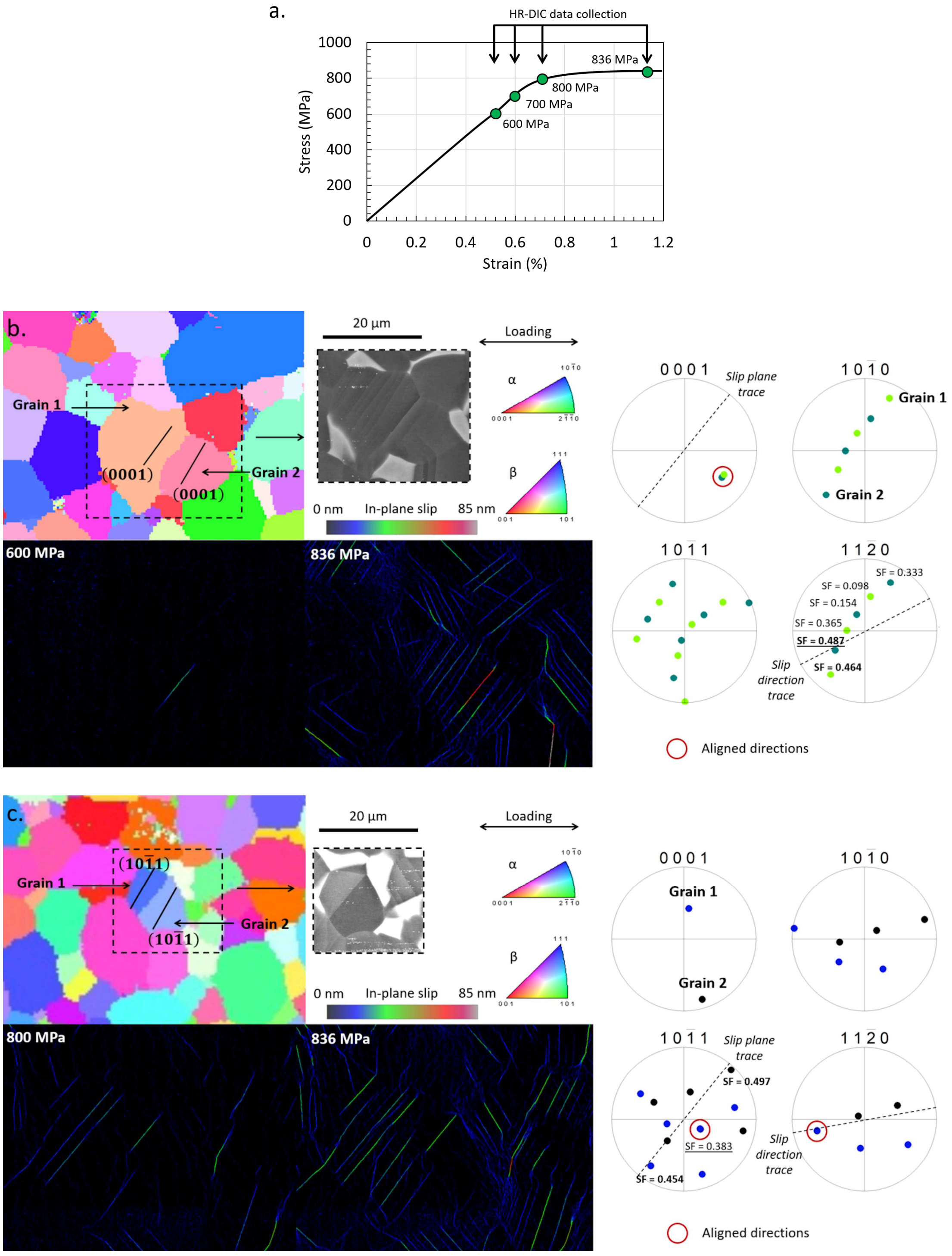

Figure 3: a. Reconstructed stress – strain curve showing stops performed for HR-DIC data collection in Ti-64E, b. and c. show crystallographic orientations along the loading direction, a backscattered electron micrograph, in-plane slip magnitudes as obtained via HR-DIC and discrete pole figures showing the orientation in grains adjacent to b. a (0001) twist boundary and c. a $\{10\bar{1}1\}$ twist boundary. The loading

direction is horizontal. Z-contrast in back-scattered electron micrographs show the arrangements of α and β phases. Maximum Schmid factors (SF) are indicated in black and the one consistent with the experimentally determined slip plane and direction is underlined.

3. Results

3.1 Fatigue behavior

Significant plastic strains accumulated during fatigue testing, as shown in Figure 2b. This feature indicates widespread plasticity in the material that is characteristic of low cycle fatigue [52]. The rate of plastic strain accumulation decreased upon cycling for all alloys, microstructure and loading conditions, except for Ti-64E. This behavior is most likely related to the noticeable but limited strain softening that occurs beyond yielding for this material, as shown in the tensile stress – strain curves presented in figure 1c. Tests were stopped prior to specimen failure after 1000 to 5000 cycles. Gage length examination revealed the presence of a few small cracks per specimen. Some tests on Ti-6242 and Ti-6246 were repeated and have led to similar numbers of initiated cracks, suggesting that the investigated area is sufficient to be representative. The fatigue lifetime of Ti-64BM was assessed in [37] with the same testing conditions as applied in the present work at a peak stress equivalent to 90 % of the yield strength. Cracks were readily observed after 1300 cycles, while complete failure of the specimens occurred after 10800 cycles on average. Therefore, crack growth consumes most of the fatigue lifetime in the investigated regime. A complete summary of testing conditions including the number of initiated cracks is given in table 4. For the applied testing conditions, the number of initiated cracks ranged between 1 and 4 ensuring that the very first initiated cracks are examined in the present study, at the most critical microstructural arrangements. Their length was lower than a few primary α grain diameters also ensuring that the identification of the initiation site is straightforward.

Material	Regime	Peak stress	Number of cycles	Location	Frequency	Presence of (0001) TB
Ti-6242	LCF	95 % YS	1000	Surface	0.25 Hz	2/2 + 2/2
Ti-6242	LCF	90 % YS	2500	Surface	0.25 Hz	2/2
Ti-6246	LCF	95 % YS	2500	Surface	0.25 Hz	4/4 + 4/4
Ti-6246	LCF	92.5 % YS	2500	Surface	0.25 Hz	1/1

Ti-64E	**LCF**	**90 % YS**	**1000**	**Surface**	**0.25 Hz**	**2/2**
Ti-64MTR	**LCF**	**87.5 % YS**	**3000**	**Surface**	**0.25 Hz**	**1/1**
Ti-64MTR	**LCF**	**90 % YS**	**1500**	**Surface**	**0.25 Hz**	**1/1**
Ti-64BM	**LCF**	**85 % YS**	**5000**	**Surface**	**0.25 Hz**	**2/2**
Ti-64BM	**LCF**	**87.5 % YS**	**2000**	**Surface**	**0.25 Hz**	**1/1**
Ti-64BM	**LCF**	**90 % YS**	**1300**	**Surface**	**0.25 Hz**	**2/2**
Ti-64BM	**LCF**	**90 % YS**	**2500**	**Surface**	**0.25 Hz**	**40/45** [37]
Ti-64BM	**LCDF**	**90 % YS**	**941**	**Sub-surface**	**0.008 Hz**	**18/20** [37]

Table 4: Summary of fatigue tests and identified fatigue cracks. LCF and LCDF indicate low cycle fatigue and low cycle dwell fatigue respectively. XX/XX indicates the ratio of the number of cracks initiated at (0001) twist boundaries (TB) to the total number of cracks. Data corresponding to several specimens are separated with +. All first cracks form in relation to (0001) twist boundaries. Results from [37] **are also indicated.**

3.2 Microstructural features at crack nucleation sites

A total of 24 cracks have been detected and characterized using SEM and EBSD. As similar features have been obtained for all alloys, microstructures and loading conditions, they are presented together in the following. SEM micrographs and local crystallographic orientation maps for a typical crack in each material are shown in figure 4. Comparison of SEM micrographs with crystallographic orientation data shows that all cracks are aligned with the basal plane trace on both sides of the cracks. Examination of orientation relationships between both sides of the cracks have revealed a misorientation about the [0001] axis at the crack initiation sites. Grain boundaries with [0001] misorientations are indicated in white in figure 4. A substantial fraction of the associated grain boundary length is not aligned with basal plane traces. As shown in figure 5, TSEM imaging of thin foils containing nucleated cracks confirms that the cracks are parallel to the basal planes. While EBSD characterization before lift out preparation demonstrated a [0001] misorientation across the crack, no boundary is visible on the micrographs. These observations reveal that cracks formed along the boundary, which is parallel to basal planes. Cracked boundaries are therefore identified as (0001) twist boundaries. All cracks extend along the entire length of the (0001) twist boundaries. This feature suggests fast crack extension along such grain boundary segments. Dislocation structures visible nearby the crack in figure 5d testify of a certain plastic activity involved in this cracking process.

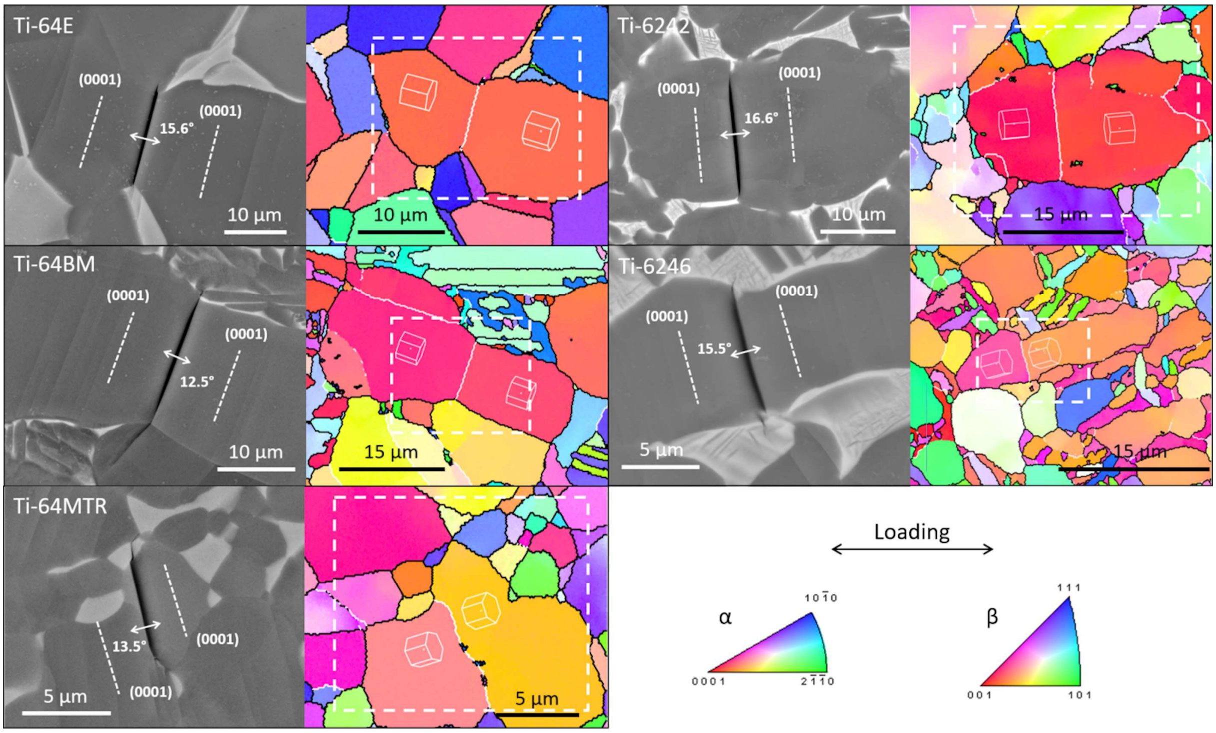

Figure 4: SEM micrographs and inverse pole figure maps showing the microstructure and the crystallographic orientations surrounding the cracks. Crystallographic orientations are along the loading direction. Basal plane traces and misorientation between both sides of the cracks are presented. Grain boundaries with $[\mathbf{0001}]$ misorientations are indicated with white lines.

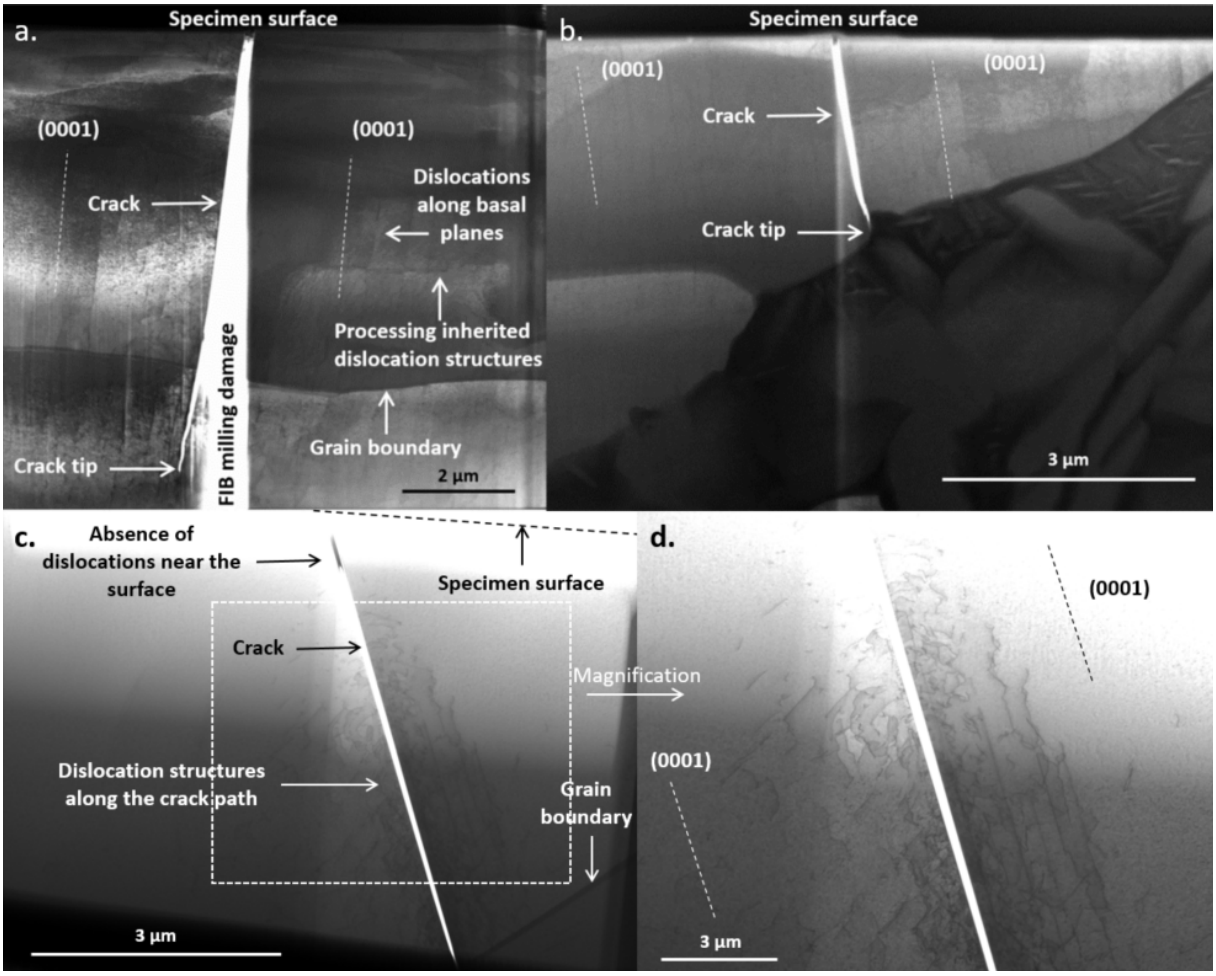

Figure 5: Bright field TSEM micrograph of a crack initiated in a. Ti-6242, b. Ti-6246 and c. Ti-64E. d. Magnification of the central region shown in c. Basal plane traces are indicated and show that the cracks coincide with the basal planes in α grains adjacent to the cracks.

The distribution of misorientation values between both sides of the cracks is shown in figure 6a. Despite the limited number of investigated cracks per material, similar trends are observed. The overall maximum frequency is reached in the 10°-15° interval. The average twist angle is 15.0°. The crack opening measured on thin foils is lower than 2°, and thus rules out a potential misorientation resulting from the cracking process alone. Crystallographic orientations on both sides of the cracks are reported in figure 6b. They show that a similar and restricted crystallographic orientation domain governs crack nucleation in the investigated materials. The comparison with Schmid factor iso-contours plotted in [53] reveals that these orientations are associated with a high Schmid factor for basal slip and lower Schmid factors for prismatic and pyramidal slip. The misorientation between the c-axis of the HCP lattice and the loading direction as well as the maximum Schmid factor for basal slip are shown in figure 6c. Most of the α grains exhibit a misorientation between the c-axis of the HCP lattice and the loading direction in the 20° - 50° range and a maximum Schmid factor for basal slip higher than 0.3. In average, the maximum Schmid factor for basal slip is 0.414 and the misorientation between the c-axis of the HCP lattice and the loading direction is 33.8°. The combination of a high Schmid factor for basal slip and misorientation values generally lower than 45° reveals the requirement of both high resolved shear stress and normal stress acting on the basal plane for crack formation. The frequent observation of basal slip traces in the initiation α grain pair is consistent with this analysis.

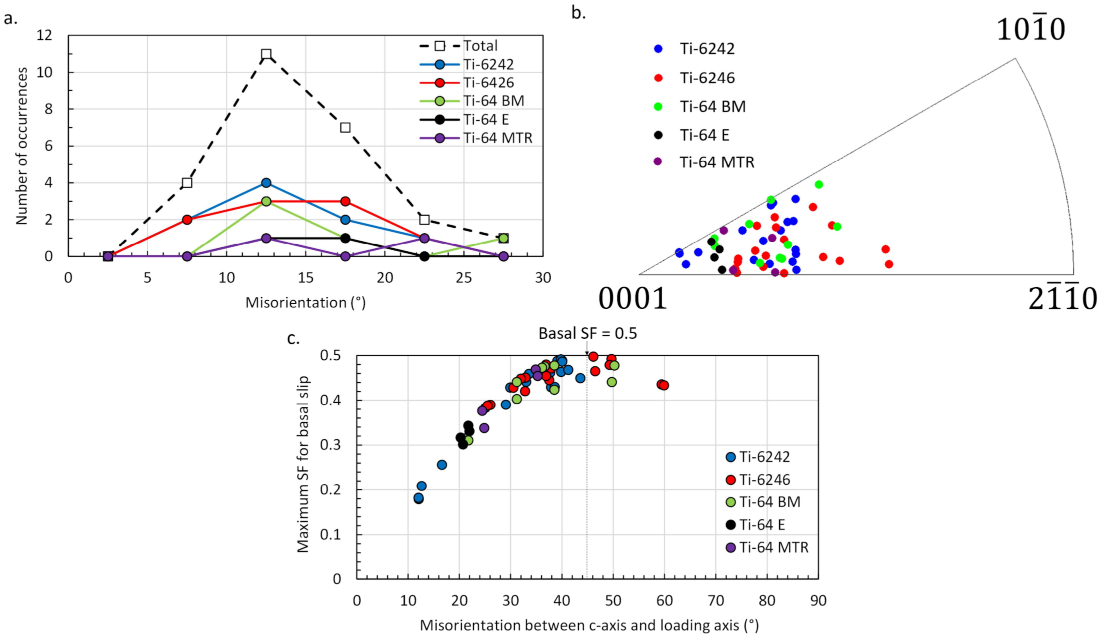

Figure 6: a. Distribution of the misorientation values between both sides of the crack, showing that cracks are most frequently formed at (0001) twist boundaries with a misorientation in the 10° and 15° range, b. Inverse pole figure plot showing the crystallographic orientation of the α grains adjacent to cracked (0001) twist boundaries along the loading direction and c. Maximum Schmid factor for basal slip plotted as a function of the misorientation between the c-axis and the loading axis, showing that α grains favoring crack formation experience a high resolved shear stress for basal slip and a high stress normal to the basal plane.

3.3 Strain localization along (0001) *and other twist boundaries using HR-DIC*

Characterization of nucleated cracks has brought substantial evidence of a key role of (0001) twist boundaries in the crack formation process. Strain localization at these specific microstructural configurations was investigated using in-situ SEM HR-DIC during a tensile test. This technique allows a reliable detection of localized slip at interfaces or boundaries [47], which can be challenging using conventional SEM observation of slip traces due to contrasts stemming from crystallographic or composition heterogeneities. In-plane slip measurements over roughly 1 mm^2 were carried out on Ti-64E at applied stress levels below the 0.5 % proof strength. Maps showing the crystallographic orientations and the in-plane slip magnitudes at each loading step are presented in figure 7. For clarity purposes, only one out of the two regions of interest is shown in this figure, but analyses and discussions include both. Additional BSE micrographs were used to ensure that slip was located at the boundary as the 0.4 µm step size associated with the EBSD scan may not provide sufficient spatial resolution. Strain localization along (0001) twist boundaries is observed. An example is presented in figure 3b. As shown on the pole figure plots, the boundary trace is parallel to the basal planes traces in the adjacent grain pair. Due to rotation around the c-axis, $\langle 11\bar{2}0\rangle$ slip directions between both sides of the boundary are not aligned but they are contained in the common (0001) plane. The slip direction derived from DIC data is consistent with the crystallographic $\langle 11\bar{2}0\rangle$ slip direction associated with the maximum Schmid factor.

Grain boundaries with $[0001]$ misorientations account for approximately 2.5% of the total grain boundary length in the investigated region. However, as illustrated in figure 4, a substantial fraction of such boundaries are not aligned with basal planes and no systematic strain localization was observed at these boundaries. In addition, strain localization was also occasionally observed along $\{10\bar{1}1\}$ twist boundaries. An example is presented in figure 3c. The boundary is parallel to a pyramidal plane trace. Furthermore, the pole figure plots show that the $(10\bar{1}1)$ slip plane which serves as the boundary plane and the associated $[1\bar{2}10]$ direction are aligned in both surrounding α grains. The slip direction derived from DIC data is consistent with slip along this $[1\bar{2}10]$ direction. A 55.7° misorientation is measured across the boundary. It is noteworthy that such orientation relationship corresponds to a $\{10\bar{1}1\}\langle 10\bar{1}2\rangle$ twin boundary [54]. Due to the considerable population of boundaries contained in the region of interest and the irrelevant character of most of them regarding fatigue crack initiation, the following analyses are focused on (0001) twist boundaries.

At the first loading step (600 MPa), only a few sparse slip events are identified. This is illustrated in figure 7. 2 out of a total of 7 slip traces are located at (0001) twist boundaries. As shown in the in-plane slip distribution frequency calculated using 0.22 nm bins and presented in figure 8a, the maximum in-plane slip magnitude was reached at these specific microstructural configurations. At higher applied stress values, a few additional slip events are located at (0001) twist boundaries but most of them correspond to intragranular basal and prismatic slip. Considering the number of slip traces included in the considered regions, no systematic identification of active slip systems was carried out. Interestingly, the maximum in-plane slip values are not located at these specific microstructural configurations at higher applied stress levels. This is shown in the in-plane slip distribution frequencies presented in figure 8a and illustrated in figure 7. At the final step, which corresponds to an applied load equivalent to 836 MPa, seven (0001) twist boundary segments were found associated with strain localization. Therefore, roughly 10^{-6} of the total grain boundary length, or 10^{-4} of grain boundaries with $[0001]$ misorientations, are (0001) twist boundaries exhibiting localized slip. Such microstructural configurations are thus very rare, and can only be captured by investigating large fields of view (≥ 1 mm^2).

Correlations between the in-plane slip magnitude and microstructural features were examined to identify critical configurations. The maximum Schmid factor for basal slip, the misorientation across the boundary, the misorientation between the c-axis of the HCP lattice and the loading direction and the measured slip length at the final loading step are plotted against the maximum in-plane slip magnitude reached along the (0001) twist boundary in figure 8b and 8c. Linear regressions were used to highlight any correlation. R^2 values indicate that only the slip length measured on the DIC maps is significantly correlated with the in-plane slip magnitude. High slip length seemingly promotes high in-plane slip values. It is worth noting that the highest in-plane slip values correspond to slip bands extending across several microstructural elements. However, considering the quite low number of observations, these trends deserve to be examined further in future work.

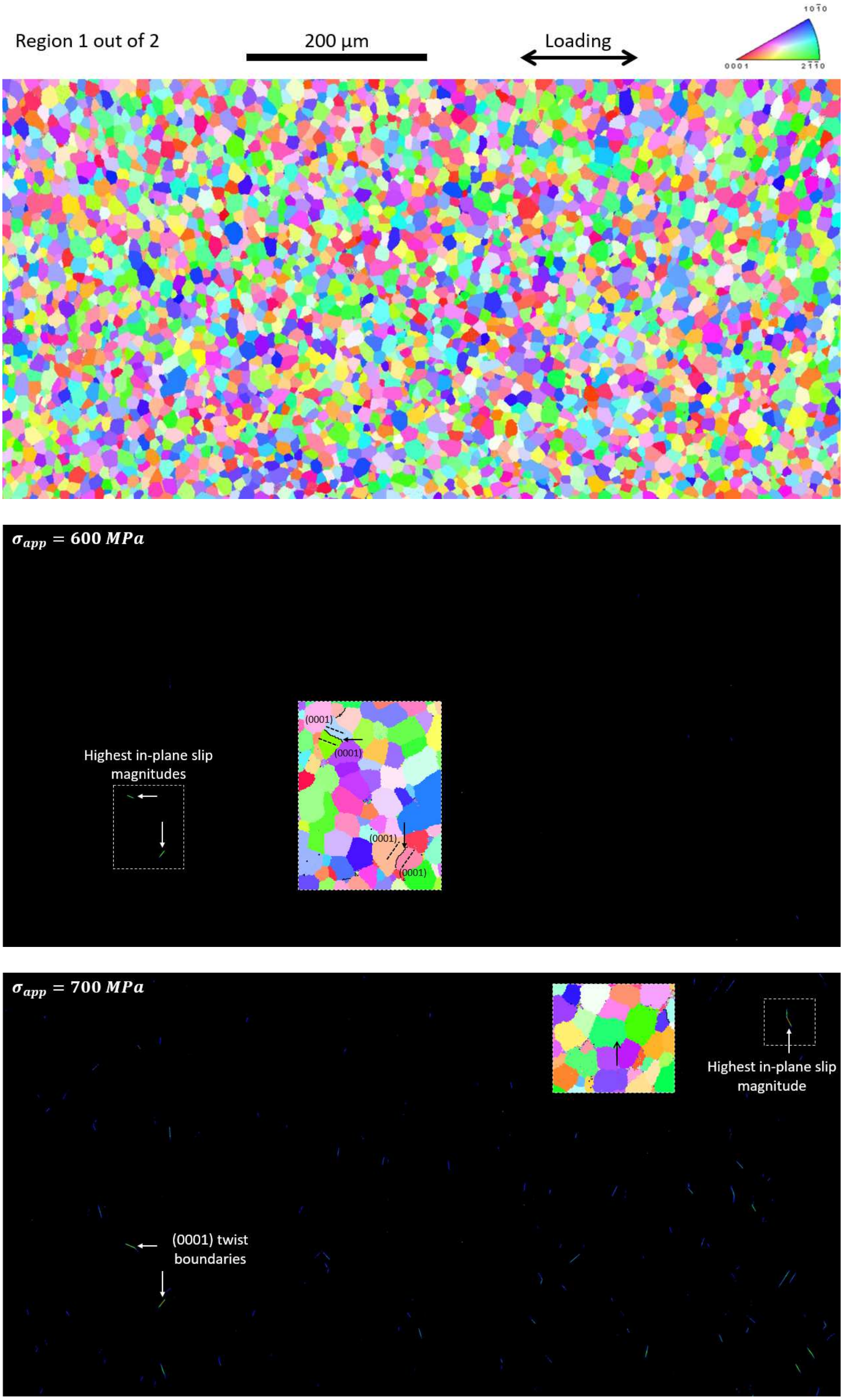
Region 1 out of 2
200 µm
Loading
10$\bar{1}$0
0001
2$\bar{1}\bar{1}$0
$\sigma_{app} = 600\ MPa$
Highest in-plane slip magnitudes
(0001)
(0001)
(0001)
(0001)
$\sigma_{app} = 700\ MPa$
Highest in-plane slip magnitude
(0001) twist boundaries

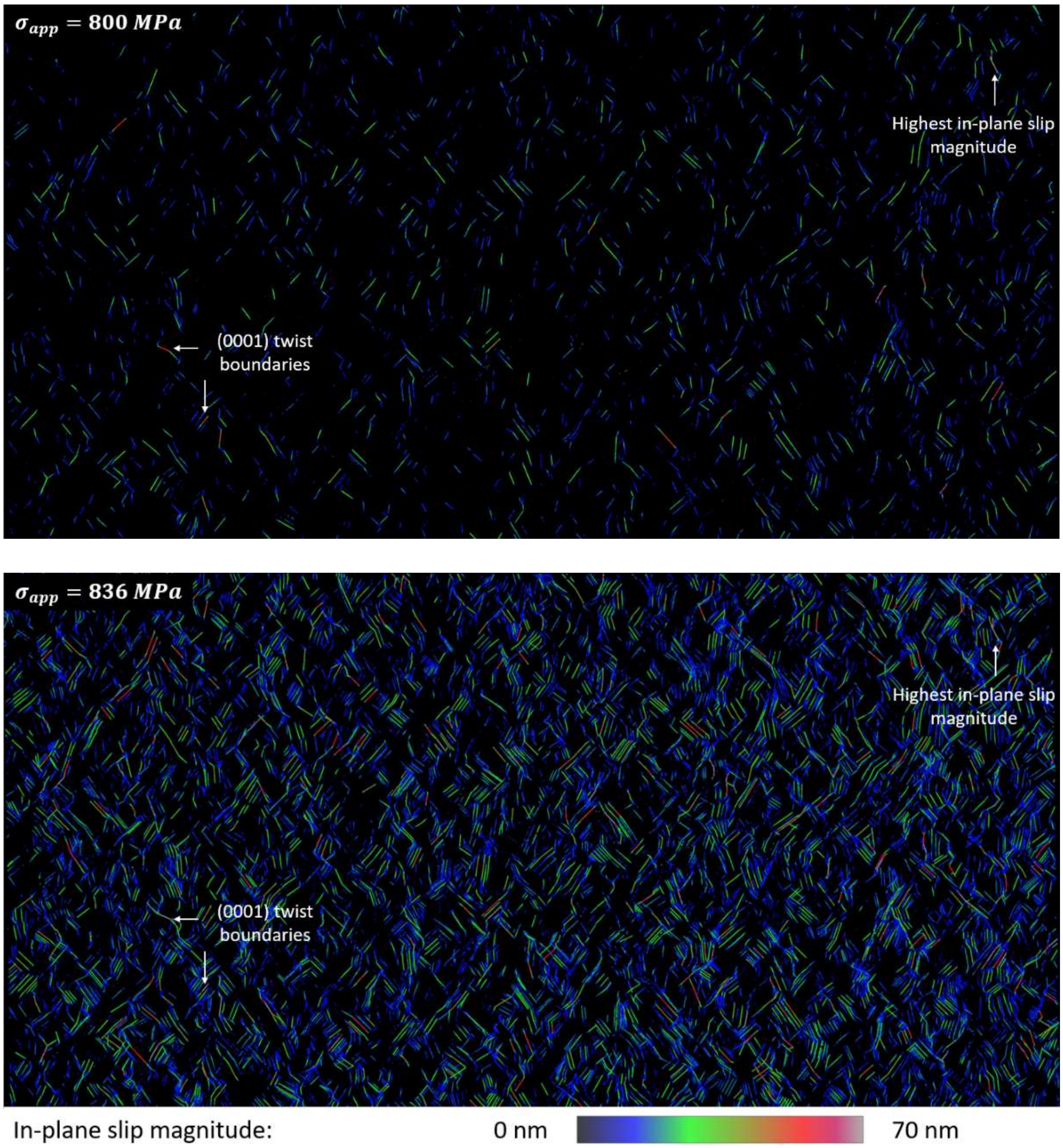

Figure 7: Crystallographic orientations along the loading direction and in-plane slip maps at the different loading steps in Ti-64E showing that most intense in-plane slip values are reached at (0001) twist boundaries at the first step (600 MPa). At higher applied stress values, highest in-plane slip values are not located at these microstructural configurations. Grain boundaries with $[\mathbf{0001}]$ misorientations are indicated with black lines in inserted IPF maps.

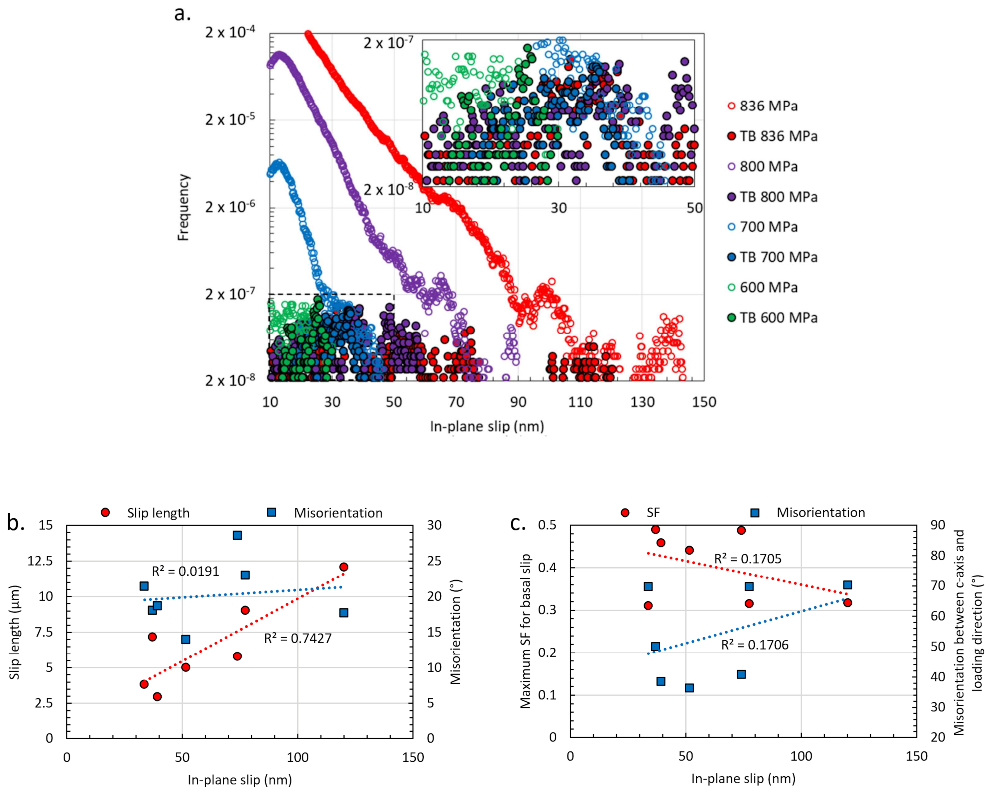

Figure 8: a. Distribution frequency of in-plane slip for overall slip activity (empty symbols) and located at (0001) twist boundaries (full symbols indicated with TB) at each loading step in Ti-64E, b. and c. show the correlation between the in-plane slip magnitude reached at each (0001) twist boundary where strain localization was observed and the slip length, the misorientation across the boundary, the maximum Schmid factor (SF) for basal slip in adjacent α grains and the misorientation between the c-axis of the HCP lattice and the loading direction. R² values indicate that significant correlation was found only with the slip length.

3.4 TEM characterization of deformation at (0001) twist boundaries

Transmission electron microscopy imaging was carried out on a thin foil extracted at a (0001) twist boundary associated with localized slip. The sample had been loaded in tension up to 0.2 % plastic strain before FIB milling. A backscattered electron micrograph and corresponding local crystallographic orientations along the loading direction nearby the boundary of interest are presented in figure 9. Bright field (BF) STEM images of the thin foil are also shown. The micrographs demonstrate that the boundary is planar. No β layer can be distinguished. No dislocation structure is visible nearby the boundary while a 22 nm high step on the surface provide evidence of the occurrence of slip. Therefore, the offset associated with localization seemingly occurred along the grain boundary. Convergent Beam Electron Diffraction (CBED) analyses were used to obtain accurate assessment of the misorientation between basal planes across the boundary. CBED patterns presented in figure 9 show the shift of the Kikkuchi line associated with the basal plane which indicates a misorientation of 1.04°.

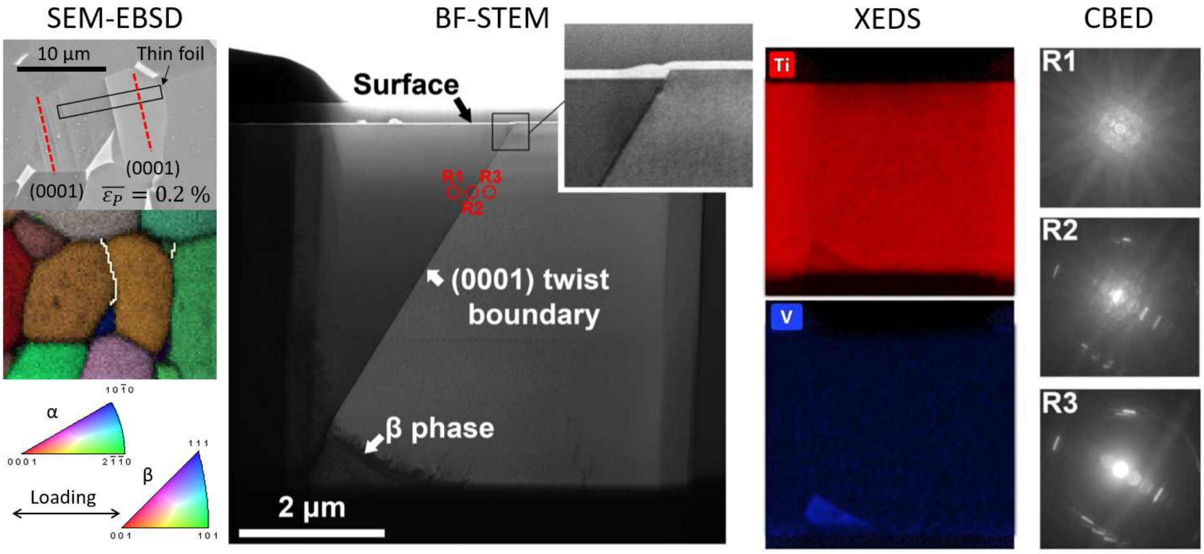

Figure 9: SEM micrograph showing the location of the thin foil, the corresponding crystallographic orientations along the loading direction where grain boundaries with $[0001]$ misorientation are indicated with white lines, BF-STEM micrographs showing shear localized at a planar (0001) twist boundary, X-EDS maps of Ti and V suggesting no composition heterogeneities at the boundary and CBED patterns showing a 1.04° misorientation between basal planes

Although SEM and BF-STEM micrographs have not provided evidence of the presence of β phase at the boundary, further confirmation was acquired using STEM-EDS. Elemental composition maps are presented in figure 9. The analyses show that β phase located at the bottom of the foil is V and Fe rich and depleted in Ti and Al. In contrast, no segregation could be evidenced at the boundary. This suggests that no β is present at the boundary. Additional evidence of the absence of β was obtained using HR-STEM characterization. A high angle annular dark field (HAADF) micrograph is presented in figure 10. The α grain on the right exhibits a $\langle 11\bar{2}0\rangle$ zone axis as determined using the fast-Fourier transform of the micrograph. The basal plane appears parallel to the boundary. This is clearly illustrated in the inverse fast Fourier transform image obtained with the $\{0002\}$ spot showing the stacking of basal planes.

Considering the grain boundary length examined in this micrograph, this observation is not inconsistent with the very low misorientation between c-axes noticed above. No specific atomic arrangement suggesting the presence of β is evidenced at the boundary. However, α/β interfaces can be difficult to detect with a $\langle 11\bar{2}0\rangle$ zone axis, when this α direction is aligned with a $\langle 110\rangle$ β direction [55] such as possibly resulting from Burgers orientation relationships [56]. A hexagonal center-of-symmetry parameter defined in [57] and previously used in [58] was calculated for each atomic column in order to highlight differences in atomic structure between both phases. While the parameter is theoretically zero when viewing the (110) β plane, it should be equal to 13.05 $\dot{A}^2$ in the $(11\bar{2}0)$ α plane. The values are plotted in the map of figure 10c. The lack of values close to zero reveals the absence of β in the investigated region. Higher values are reached close to the boundary indicating distortions in the lattice structure. A similar characterization (not presented here) was carried out on the grain on the other side of the investigated boundary and similar results were obtained.

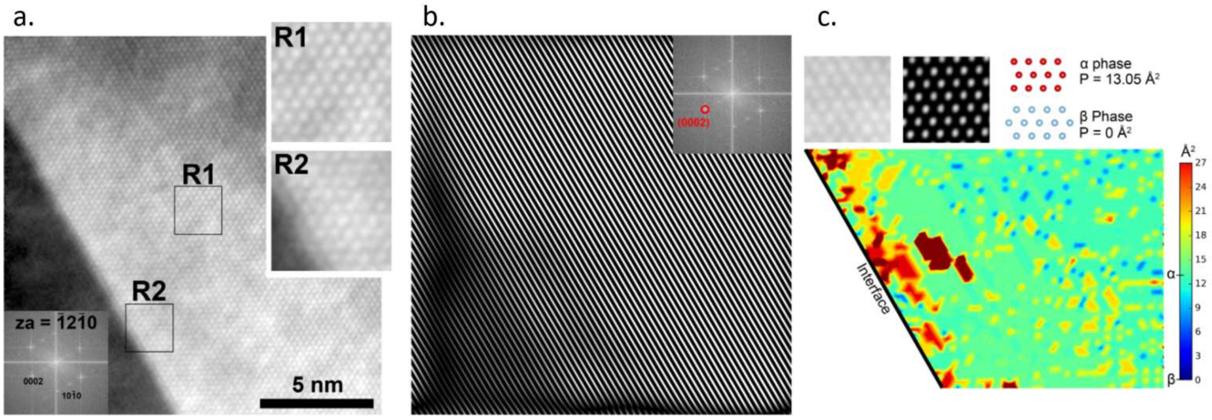

Figure 10: High-resolution HAADF-STEM images along the $\langle 11\bar{2}0\rangle$ zone axis of the crystal on the right: a. The HR-STEM image with inserts showing magnifications of R1 and R2 regions and a fast Fourier transform of the entire image, b. The inverse fast Fourier transform image of the entire region in a. when selecting the {0002} spot in the FFT as labeled, and c. Map of the hexagonal center-of-symmetry parameter (P). The absence of values close to zero indicates that no β is present in the investigated region.

4. Discussion

4.1 Fatigue crack initiation in Ti alloys

In the present study, room temperature low-cycle fatigue tests have been carried out using several alloys, microstructures and loading conditions. They were stopped after formation of a restricted number of small cracks, ensuring the analysis of the most critical microstructural configurations regarding crack initiation in Ti alloys. All observations have demonstrated that early cracks are formed on (0001) twist boundaries separating equiaxed α grains well oriented for basal slip. The twist boundaries, which are parallel to the basal planes in the surrounding grain pair, experience a high resolved shear stress. Basal slip activity is often observed in the grain pair surrounding the boundary, however, this is not systematic. Prismatic slip traces are occasionally observed in these grains as well. Based on surface SEM and cross-sectional TSEM observations, these plasticity events do not seem to be directly involved in the crack formation process. It is worth noting that stiff oriented grains seem more favorable for crack formation, which may result from a higher stress induced by the high directional modulus [7,59]. As observed cracks systematically extended along the entire length of the (0001) twist boundary, crack extension along these grain boundary segments appears to be fast.

The similar features observed at crack nucleation sites for all materials considered in the present study reveal the operation of a unique crack formation mechanism. This finding provides interesting insights into the effects of composition and microstructure. While equivalent aluminum contents are around 8 wt. % for all considered alloys, the equivalent molybdenum content ranges from 2 to 6 wt. % [56]. Different β phase fractions result from the different amounts of β stabilizing elements. In particular, Ti-6Al-2Sn-4Zr-XMo alloys (with X = 2 or 6) do not contain V, which is the only major β stabilizing element in Ti-6Al-4V. In these alloys, Mo is the main β stabilizing species and exhibits a lower diffusivity than V. The alloying elements significantly differ in the α phase a well. Only Al is expected to be present in similar amounts. The oxygen content in Ti-6Al-2Sn-4Zr-XMo alloys used in the present study is lower than in Ti-6Al-4V alloys. α grains in Ti-6Al-2Sn-4Zr-XMo contain several weight percents of Zr and Sn [43] while a few weight percents of V are present in Ti-6Al-4V [60]. It is interesting to notice that α phase in Ti-6Al-2Sn-4Zr-XMo alloys have roughly the same composition [43]. In spite of these numerous differences, (0001) twist boundaries were present in all investigated materials and the crack nucleation mechanism was observed to be insensitive to the average and local composition variations. Microstructural features, such as the α grain size, the lamellas thicknesses or the degree of microtexture, have not induced a change in mechanism either. This may have occurred due to a different pattern of strain partitioning between the metallurgical constituents. As none of these variations has modified the (0001) twist boundary crack nucleation mechanism presently observed, it seems to have a broad relevance for Ti alloys subjected to cyclic loading. A similar mechanism was found to operate for surface and subsurface dwell-fatigue crack nucleation [37]. No mechanism change stems from the differences in stress state and environmental effects due to the free surface. The variety of applied loading conditions has not resulted in a mechanism change either. Additional investigations are on-going to clarify how the present findings translate to different loading conditions including high cycle fatigue or complex loading paths such as experienced in-service.

The presently reported findings question the consistency with prior studies mentioned in the introductory section. It is clear that no plastic deformation event in a neighboring α grain triggers crack formation and cracks do not initiate in a "hard" grain, i.e. where basal or prismatic slip is difficult, as opposed to the mechanism proposed by Evans and Bache for dwell-fatigue crack initiation [61]. However, features of the grains adjacent to the cracks such as a high Schmid factor for basal slip and a low misorientation between the c-axis of the HCP lattice and the loading direction are consistent with data from prior studies where cracks were reported to initiate on an intragranular basal slip band [5,13,21]. It is noteworthy that some of the associated data have been recently revisited [37]. A (0001) twist boundary with the same features as highlighted in the present work was found at the crack initiation site. An incomplete interpretation of fracture surfaces in previous studies may arise from the analysis of failed specimens containing only half of the microstructure surrounding the cracks. The present results suggest that a careful analysis of the 3D microstructure at the crack initiation sites should be carried out in order to evidence the presence of the (0001) twist boundaries.

4.2 Localized shear at (0001) twist boundaries and transition to crack initiation

Additional analyzes were performed on Ti-6Al-4V with an equiaxed microstructure in order to unveil the preliminary deformation steps leading to crack formation. Particular attention was paid to microstructural configurations described above. The occurrence of strain localization along (0001) twist boundaries was evidenced. They constitute preferential locations for the early plastic deformation events and are associated with intense slip activity. This is especially noticeable as these microstructural configurations are very rare. A few more intense slip events were found elsewhere at higher applied stress. However, it must be kept in mind that in-plane slip is assessed, which may not reflect the out-of-plane slip component that is important regarding fatigue crack nucleation [62]. Another important feature governing the magnitude of the strain at (0001) twist boundaries is the slip length as continuous slip across several microstructural elements generates high in-plane slip values. Other boundaries such as $\{10\bar{1}1\}$ twist boundaries were found prone to strain localization as well although not observed at low stress. These boundaries are planar and contain one slip system that experiences a high resolved shear stress. Shear along twist boundaries was observed to be consistent with slip along a <a> direction contained in the boundary plane and associated with a high resolved shear stress. As these features are similar for both (0001) and $\{10\bar{1}1\}$ twist boundaries, they are likely to be required for strain localization to occur along a twist boundary.

The origin of the early slip localization at (0001) twist boundaries is still unclear. No stress concentration is expected to result from the adjacent grain configuration as HCP α exhibits a transversely isotropic elastic behavior in the basal plane. In addition, no elemental segregation, which may potentially generate a locally softer region, was detected either. This feature also suggests that no β layer is present at the boundary. This was confirmed using HR-STEM characterization of atomic arrangements in the grain boundary region. The existence of α/α grain boundaries in a dual phase Ti alloy was recently evidenced in [55]. The structure of a (0001) twist boundary was examined by Liu et al. in a fracture toughness reduction context [63,64]. The authors have reported a possible presence of β phase at the boundary using HR-TEM and electron energy loss spectroscopy. While this conclusion seems in contradiction with the present results, it is worth noting that the boundary studied in [63] was not parallel to the basal planes in adjacent grains and therefore unlikely to be a potential slip localization or crack initiation site. In the present work, the characterization of a boundary exhibiting strain localization ensured the study of a relevant microstructural region.

Although no direct evidence of crack formation on localized slip is presently reported, Lavogiez et al. have imaged the crack opening following intense strain localization at (0001) twist boundaries in Ti-64BM [37]. Shearing along (0001) twist boundaries is thus a preliminary step for crack formation. The absence of visible dislocation structures nearby the boundary suggests that these planar α/α grain boundaries are able to accommodate deformation via shearing. In contrast, crack opening along sheared twist boundaries seems accompanied by a limited yet noticeable plastic activity in the surrounding region. Several authors have reported the presence of (0001) twist boundaries in crack initiation regions, but no direct link with the crack formation mechanism was formulated to the best of the authors knowledge [65,66]. The underlying cause of premature cracking at such microstructural elements is still unclear as it does not seem to pertain to local stress concentrations or local composition variations as discussed above. The atomic structure and interfacial energy of the twist boundaries may play a key role in this process. Another question that may arise is whether other boundaries associated with shearing are prone to cracking. While it is clear that they are not associated with early crack formation, one cannot exclude cracking later in the cycling process. An additional Ti-64BM specimen was tested until multiple cracks were initiated. 2500 cycles were applied while the first cracks were readily observed after 1300 cycles for similar loading conditions. A crack was located at a $\{10\bar{1}1\}$ twist boundary. Crystallographic orientations and a SEM micrograph in the region surrounding the crack are presented in figure 11. The features exhibited by this boundary are consistent with those listed in the previous paragraphs, thus suggesting that it is suitable for strain localization. This crack further demonstrates the specific character of such boundaries regarding crack formation.

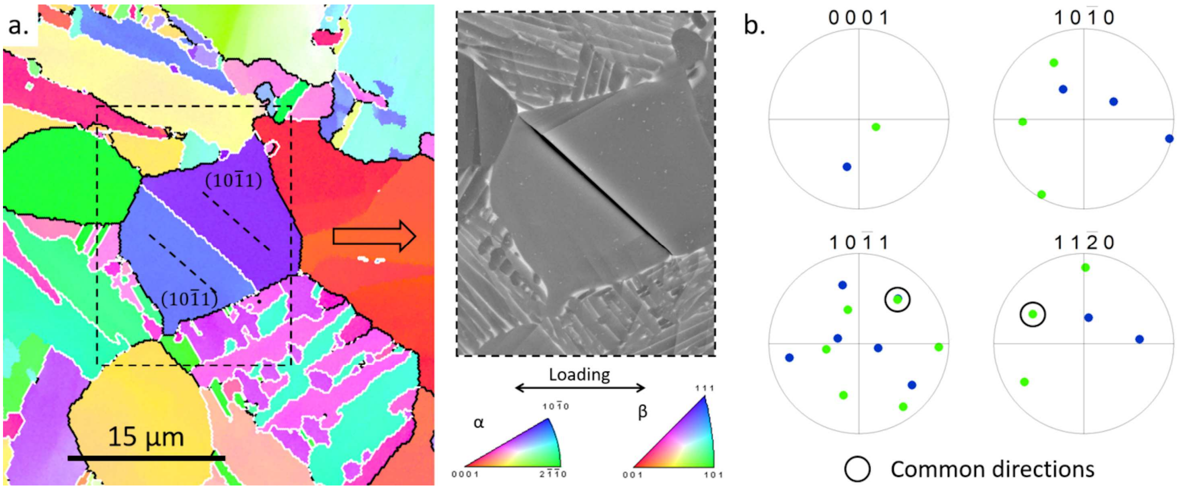

Figure 11: a. Inverse pole figure map showing the crystallographic orientation along the loading direction nearby a crack and the associated backscattered electron micrograph, b. Pole figures show that cracking occurred along a $\{10\bar{1}1\}$ twist boundary. 2500 cycles with a peak stress equivalent to 90 % of the yield strength was applied on this Ti-64BM specimen.

Microstructural configurations favorable for (0001) twist boundary shear were found to be very rare. In agreement with this finding, (0001) twist boundaries were not identified among the most common grain boundaries according to the extensive study of grain boundaries in α-Ti carried out by Kelly et al. [67]. As a consequence, they constitute the most influential microstructural feature governing crack formation and are likely to contribute to the high variability in fatigue life. This finding offers new ways of improving the understanding and the prediction of fatigue crack initiation in titanium alloys. (0001) twist boundaries are likely to form as a result of dynamic recrystallization, though this has not yet been studied in detail. Therefore, the density of (0001) twist boundaries, and thus of potential crack initiation sites, probably depends on the applied processing route. Additional complexity is expected with the extrapolation to industrial components since microstructure and stress field heterogeneities stemming from complex geometries, loadings and processing histories have to be considered. As a consequence of the scarcity of these microstructural elements, representative volume elements must be considered with a specific care. In particular, restricted volumes tested in conventional laboratory tests may to contribute to a difficult prediction of properties such as high-cycle fatigue, which is governed by the weakest-link. For instance, with less than ten (0001) twist boundaries where slip localization occurs in 1 mm^2, the region considered for HR-DIC analyses is probably insufficient to be really representative in spite of its large size. Repeated fatigue tests on Ti-6242 and Ti-6246 with similar conditions led to a similar number of cracks, suggesting that 20 mm^2 could be sufficient within the investigated set of material and testing conditions. Further complications are expected depending on the features of microtextured regions, which can induce microstructure and stress/strain field heterogeneities up to the centimeter scale. The associated challenges are likely to be overcome in the upcoming years with the advent of large scale reconstruction and efficient simulation techniques.

5. Conclusions

In summary, the mechanism of low-cycle fatigue crack formation was investigated for several titanium alloys processed to have different microstructures. Tests were carefully stopped in order to study microcracks. Deformation at potential crack initiation sites was subsequently characterized in order to unveil processes leading to crack formation. The following conclusions have been drawn:

- For all alloys, microstructures and loading conditions, a similar crack formation mechanism was observed. Insensitivity to composition as well as microstructure differences including the grain size, the degree of microtexture and the β fraction demonstrates a broad relevance of the present findings.
- Early cracks form at (0001) twist boundaries. Crack opening along such boundary segments seems fast and associated with some plastic activity in the region surrounding the boundary. In order to constitute a potential crack initiation site, the twist boundary must experience a high resolved shear stress and a high normal stress. In addition, misorientation is generally in the 10° - 20° range.
- Localized shear along (0001) twist boundaries precedes crack formation. No β layer was found using a variety of characterization techniques, suggesting that shearing proceeds along α/α grain boundaries. At such locations, strain localization is intense and occurs at low stress as compared to the majority of slip activity. These microstructural configurations are rare as (0001) twist boundaries with strain localization account for roughly 10^{-6} of the total grain boundary length. In addition, local microstructural configurations allowing a high slip length exacerbate the propensity to high slip magnitudes.
- $\{10\bar{1}1\}$ twist boundaries were also found prone to slip localization and possibly crack formation later in the cycling process. Important features of boundaries associated with strain localization and crack formation include i. the parallelism of a slip plane with the boundary and ii. a high resolved shear stress on a slip system involving this slip plane.

6. Acknowledgements

This work partially pertains to the French Government program "Investissements d'Avenir" (LABEX INTERACTIFS, reference ANR-11-LABX-0017-01). This work has been partially supported by « Nouvelle Aquitaine » Region and by European Structural and Investment Funds (ERDF reference : P-2016-BAFE-94/95). Pprime Institute gratefully acknowledges "Contrat de Plan Etat - Région Nouvelle-Aquitaine" (CPER) as well as the "Fonds Européen de Développement Régional (FEDER)" for their financial support to the reported work. JCS and TMP acknowledge the support of ONR grant N00014-19-2129.

7. CRediT author statement

S. Hémery: Conceptualization, methodology, investigation, formal analysis, visualization, writing-original draft, supervision, resources, **J.C. Stinville:** Methodology, investigation, formal analysis, visualization, writing-review and editing, supervision, **F. Wang:** Investigation, visualization, **M.A. Charpagne:** Investigation, writing-review and editing, **M. Emigh:** Investigation, **T.M. Pollock:** Supervision, resources, writing-review and editing, **V. Valle:** Resources

8. References

[1] Accident to the AIRBUS A380-861 registered F-HPJE and operated by Air France on 30/09/2017 en route over Greenland [Investigation delegated to BEA by the authorities of Denmark], (n.d.). https://www.bea.aero/en/investigation-reports/notified-events/detail/accident-to-the-airbus-a380-861-registered-f-hpje-and-operated-by-air-france-on-30-09-2017-en-route-over-greenland-investigation-delegated-to-bea-by-the-authorities-of-denmark/ (accessed January 31, 2021).

[2] M.R. Bache, A review of dwell sensitive fatigue in titanium alloys: the role of microstructure, texture and operating conditions, International Journal of Fatigue. 25 (2003) 1079–1087. https://doi.org/10.1016/S0142-1123(03)00145-2.

[3] F.P.E. Dunne, D. Rugg, A. Walker, Lengthscale-dependent, elastically anisotropic, physically-based hcp crystal plasticity: Application to cold-dwell fatigue in Ti alloys, International Journal of Plasticity. 23 (2007) 1061–1083. https://doi.org/10.1016/j.ijplas.2006.10.013.

[4] D. Ozturk, A.L. Pilchak, S. Ghosh, Experimentally validated dwell and cyclic fatigue crack nucleation model for α–titanium alloys, Scripta Materialia. 127 (2017) 15–18. https://doi.org/10.1016/j.scriptamat.2016.08.031.

[5] A.L. Pilchak, J.C. Williams, Observations of Facet Formation in Near-α Titanium and Comments on the Role of Hydrogen, Metall Mater Trans A. 42 (2011) 1000–1027. https://doi.org/10.1007/s11661-010-0507-9.

[6] Y. Liu, F.P.E. Dunne, The Mechanistic Link between Macrozones and Dwell Fatigue in Titanium Alloys, International Journal of Fatigue. (2020) 105971. https://doi.org/10.1016/j.ijfatigue.2020.105971.

[7] S. Hémery, A. Naït-Ali, M. Guéguen, J. Wendorf, A.T. Polonsky, M.P. Echlin, J.C. Stinville, T.M. Pollock, P. Villechaise, A 3D analysis of the onset of slip activity in relation to the degree of micro-texture in Ti–6Al–4V, Acta Materialia. 181 (2019) 36–48. https://doi.org/10.1016/j.actamat.2019.09.028.

[8] Azdine.Nait-Ali, S. Hémery, M. Gueguen, How macrozone size and morphology influence yield in titanium alloys investigated using fast Fourier transform-based crystal plasticity simulations, International Journal of Solids and Structures. (2021). https://doi.org/10.1016/j.ijsolstr.2021.01.008.

[9] J. Cappola, J.-C. Stinville, M.-A. Charpagne, P.G. Callahan, M.P. Echlin, T.M. Pollock, A. Pilchak, M. Kasemer, On the Localization of Plastic Strain in Microtextured Regions of Ti-6Al-4V, Acta Materialia. (2020) 116492. https://doi.org/10.1016/j.actamat.2020.116492.

[10] C.P. Przybyla, D.L. McDowell, Simulated microstructure-sensitive extreme value probabilities for high cycle fatigue of duplex Ti–6Al–4V, International Journal of Plasticity. 27 (2011) 1871–1895. https://doi.org/10.1016/j.ijplas.2011.01.006.

[11] D.L. McDowell, Simulation-based strategies for microstructure-sensitive fatigue modeling, Materials Science and Engineering: A. 468–470 (2007) 4–14. https://doi.org/10.1016/j.msea.2006.08.129.

[12] S.K. Jha, C.J. Szczepanski, P.J. Golden, W.J. Porter, R. John, Characterization of fatigue crack-initiation facets in relation to lifetime variability in Ti–6Al–4V, International Journal of Fatigue. 42 (2012) 248–257. https://doi.org/10.1016/j.ijfatigue.2011.11.017.

[13] V. Sinha, A.L. Pilchak, S.K. Jha, W.J. Porter, R. John, J.M. Larsen, Correlating Scatter in Fatigue Life with Fracture Mechanisms in Forged Ti-6242Si Alloy, Metall Mater Trans A. 49 (2018) 1061–1078. https://doi.org/10.1007/s11661-017-4437-7.

[14] C.J. Szczepanski, S.K. Jha, J.M. Larsen, J.W. Jones, Microstructural Influences on Very-High-Cycle Fatigue-Crack Initiation in Ti-6246, Metall Mater Trans A. 39 (2008) 2841–2851. https://doi.org/10.1007/s11661-008-9633-z.

[15] K. Kirane, S. Ghosh, A cold dwell fatigue crack nucleation criterion for polycrystalline Ti-6242 using grain-level crystal plasticity FE Model, International Journal of Fatigue. 30 (2008) 2127–2139. https://doi.org/10.1016/j.ijfatigue.2008.05.026.

[16] B. Chen, J. Jiang, F.P.E. Dunne, Is stored energy density the primary meso-scale mechanistic driver for fatigue crack nucleation?, International Journal of Plasticity. 101 (2018) 213–229. https://doi.org/10.1016/j.ijplas.2017.11.005.

[17] S. Joseph, T.C. Lindley, D. Dye, Dislocation interactions and crack nucleation in a fatigued near-alpha titanium alloy, International Journal of Plasticity. 110 (2018) 38–56. https://doi.org/10.1016/j.ijplas.2018.06.009.

[18] X. Demulsant, J. Mendez, MICROSTRUCTURAL EFFECTS ON SMALL FATIGUE CRACK INITIATION AND GROWTH IN Ti6A14V ALLOYS, Fatigue & Fracture of Engineering Materials & Structures. 18 (1995) 1483–1497. https://doi.org/10.1111/j.1460-2695.1995.tb00870.x.

[19] J.A. Hall, Fatigue crack initiation in alpha-beta titanium alloys, International Journal of Fatigue. 19 (1997) 23–37. https://doi.org/10.1016/S0142-1123(97)00047-9.

[20] R.K. Nalla, R.O. Ritchie, B.L. Boyce, J.P. Campbell, J.O. Peters, Influence of microstructure on high-cycle fatigue of Ti-6Al-4V: Bimodal vs. lamellar structures, Metall Mater Trans A. 33 (2002) 899–918. https://doi.org/10.1007/s11661-002-0160-z.

[21] F. Bridier, P. Villechaise, J. Mendez, Slip and fatigue crack formation processes in an α/β titanium alloy in relation to crystallographic texture on different scales, Acta Materialia. 56 (2008) 3951–3962. https://doi.org/10.1016/j.actamat.2008.04.036.

[22] K.L. Biavant, S. Pommier, C. Prioul, Local texture and fatigue crack initiation in a Ti-6Al-4V titanium alloy, Fatigue & Fracture of Engineering Materials & Structures. 25 (2002) 527–545. https://doi.org/10.1046/j.1460-2695.2002.00480.x.

[23] S.G. Ivanova, R.R. Biederman, R.D. Sisson, Investigation of fatigue crack initiation in Ti-6Al-4V during tensile-tensile fatigue, J. of Materi Eng and Perform. 11 (2002) 226–231. https://doi.org/10.1361/105994902770344312.

[24] D.F. Neal, P.A. Blenkinsop, Internal fatigue origins in α-β titanium alloys, Acta Metallurgica. 24 (1976) 59–63. https://doi.org/10.1016/0001-6160(76)90147-4.

[25] G. Lütjering, Influence of processing on microstructure and mechanical properties of (α+β) titanium alloys, Materials Science and Engineering: A. 243 (1998) 32–45. https://doi.org/10.1016/S0921-5093(97)00778-8.

[26] M. Hagiwara, T. Kitashima, S. Emura, Relationship between microstructures, facet morphologies at the high-cycle fatigue (HCF) crack initiation site, and HCF strength in Ti-6242S, Materials Science and Engineering: A. 727 (2018) 43–50. https://doi.org/10.1016/j.msea.2018.04.043.

[27] S. Sasaoka, J. Arakawa, H. Akebono, A. Sugeta, Y. Shirai, E. Nakayama, Y. Kimura, The effects of crystallographic orientation on fatigue crack initiation behavior in Ti-6Al-4V, International Journal of Fatigue. 117 (2018) 371–383. https://doi.org/10.1016/j.ijfatigue.2018.07.039.

[28] F. Briffod, T. Shiraiwa, M. Enoki, Nucleation and propagation modeling of short fatigue crack in rolled bi-modal Ti–6Al–4V alloy, Materials Science and Engineering: A. 790 (2020) 139710. https://doi.org/10.1016/j.msea.2020.139710.

[29] J. Everaerts, D. Gontcharov, B. Verlinden, M. Wevers, The influence of load holds on the fatigue behaviour of drawn Ti-6Al-4V wires, International Journal of Fatigue. 98 (2017) 203–211. https://doi.org/10.1016/j.ijfatigue.2017.01.043.

[30] S. Hémery, V.T. Dang, L. Signor, P. Villechaise, Influence of Microtexture on Early Plastic Slip Activity in Ti-6Al-4V Polycrystals, Metall Mater Trans A. 49 (2018) 2048–2056. https://doi.org/10.1007/s11661-018-4569-4.

[31] S. Hémery, P. Villechaise, Comparison of slip system activation in Ti-6Al-2Sn-4Zr-2Mo and Ti-6Al-2Sn-4Zr-6Mo under tensile, fatigue and dwell-fatigue loadings, Materials Science and Engineering: A. 697 (2017) 177–183. https://doi.org/10.1016/j.msea.2017.05.021.

[32] S. Hémery, P. Villechaise, In situ EBSD investigation of deformation processes and strain partitioning in bi-modal Ti-6Al-4V using lattice rotations, Acta Materialia. 171 (2019) 261–274. https://doi.org/10.1016/j.actamat.2019.04.033.

[33] M.A. Charpagne, J.C. Stinville, P.G. Callahan, D. Texier, Z. Chen, P. Villechaise, V. Valle, T.M. Pollock, Automated and quantitative analysis of plastic strain localization via multi-modal data recombination, Materials Characterization. 163 (2020) 110245. https://doi.org/10.1016/j.matchar.2020.110245.

[34] Z. Zhang, T.-S. Jun, T.B. Britton, F.P.E. Dunne, Intrinsic anisotropy of strain rate sensitivity in single crystal alpha titanium, Acta Materialia. 118 (2016) 317–330. https://doi.org/10.1016/j.actamat.2016.07.044.

[35] I. Bantounas, D. Dye, T.C. Lindley, The effect of grain orientation on fracture morphology during high-cycle fatigue of Ti–6Al–4V, Acta Materialia. 57 (2009) 3584–3595. https://doi.org/10.1016/j.actamat.2009.04.018.

[36] K. Tanaka, T. Mura, A Dislocation Model for Fatigue Crack Initiation, Journal of Applied Mechanics. 48 (1981) 97–103. https://doi.org/10.1115/1.3157599.

[37] C. Lavogiez, S. Hémery, P. Villechaise, On the mechanism of fatigue and dwell-fatigue crack initiation in Ti-6Al-4V, Scripta Materialia. 183 (2020) 117–121. https://doi.org/10.1016/j.scriptamat.2020.03.031.

[38] N.E. Paton, R.A. Spurling, Hydride habit planes in titanium-aluminum alloys, Metall Mater Trans A. 7 (1976) 1769–1774. https://doi.org/10.1007/BF02817895.

[39] K. Zhang, K.V. Yang, A. Huang, X. Wu, C.H.J. Davies, Fatigue crack initiation in as forged Ti–6Al–4V bars with macrozones present, International Journal of Fatigue. 80 (2015) 288–297. https://doi.org/10.1016/j.ijfatigue.2015.05.020.

[40] V. Hasija, S. Ghosh, M.J. Mills, D.S. Joseph, Deformation and creep modeling in polycrystalline Ti–6Al alloys, Acta Materialia. 51 (2003) 4533–4549. https://doi.org/10.1016/S1359-6454(03)00289-1.

[41] S. Joseph, K. Joseph, T.C. Lindley, D. Dye, The role of dwell hold on the dislocation mechanisms of fatigue in a near alpha titanium alloy, International Journal of Plasticity. 131 (2020) 102743. https://doi.org/10.1016/j.ijplas.2020.102743.

[42] Y. Xu, S. Joseph, P. Karamched, K. Fox, D. Rugg, F.P.E. Dunne, D. Dye, Predicting dwell fatigue life in titanium alloys using modelling and experiment, Nature Communications. 11 (2020) 5868. https://doi.org/10.1038/s41467-020-19470-w.

[43] J. Qiu, Y. Ma, J. Lei, Y. Liu, A. Huang, D. Rugg, R. Yang, A Comparative Study on Dwell Fatigue of Ti-6Al-2Sn-4Zr-xMo (x = 2 to 6) Alloys on a Microstructure-Normalized Basis, Metall Mater Trans A. 45 (2014) 6075–6087. https://doi.org/10.1007/s11661-014-2541-5.

[44] M.M. Attallah, S. Zabeen, R.J. Cernik, M. Preuss, Comparative determination of the α/β phase fraction in α+β-titanium alloys using X-ray diffraction and electron microscopy, Materials Characterization. 60 (2009) 1248–1256. https://doi.org/10.1016/j.matchar.2009.05.006.

[45] J.W. Elmer, T.A. Palmer, S.S. Babu, E.D. Specht, In situ observations of lattice expansion and transformation rates of α and β phases in Ti–6Al–4V, Materials Science and Engineering: A. 391 (2005) 104–113. https://doi.org/10.1016/j.msea.2004.08.084.

[46] A.D. Kammers, S. Daly, Self-Assembled Nanoparticle Surface Patterning for Improved Digital Image Correlation in a Scanning Electron Microscope, Exp Mech. 53 (2013) 1333–1341. https://doi.org/10.1007/s11340-013-9734-5.

[47] J.C. Stinville, M.P. Echlin, D. Texier, F. Bridier, P. Bocher, T.M. Pollock, Sub-Grain Scale Digital Image Correlation by Electron Microscopy for Polycrystalline Materials during Elastic and Plastic Deformation, Exp Mech. 56 (2016) 197–216. https://doi.org/10.1007/s11340-015-0083-4.

[48] Z. Chen, W. Lenthe, J.C. Stinville, M. Echlin, T.M. Pollock, S. Daly, High-Resolution Deformation Mapping Across Large Fields of View Using Scanning Electron Microscopy and Digital Image Correlation, Exp Mech. 58 (2018) 1407–1421. https://doi.org/10.1007/s11340-018-0419-y.

[49] F. Bourdin, J.C. Stinville, M.P. Echlin, P.G. Callahan, W.C. Lenthe, C.J. Torbet, D. Texier, F. Bridier, J. Cormier, P. Villechaise, T.M. Pollock, V. Valle, Measurements of plastic localization by heaviside-digital image correlation, Acta Materialia. 157 (2018) 307–325. https://doi.org/10.1016/j.actamat.2018.07.013.

[50] V. Valle, S. Hedan, P. Cosenza, A.L. Fauchille, M. Berdjane, Digital Image Correlation Development for the Study of Materials Including Multiple Crossing Cracks, Exp Mech. 55 (2015) 379–391. https://doi.org/10.1007/s11340-014-9948-1.

[51] M.-A. Charpagne, F. Strub, T.M. Pollock, Accurate reconstruction of EBSD datasets by a multimodal data approach using an evolutionary algorithm, Materials Characterization. 150 (2019) 184–198. https://doi.org/10.1016/j.matchar.2019.01.033.

[52] D.L. McDowell, F.P.E. Dunne, Microstructure-sensitive computational modeling of fatigue crack formation, International Journal of Fatigue. 32 (2010) 1521–1542. https://doi.org/10.1016/j.ijfatigue.2010.01.003.

[53] F. Bridier, P. Villechaise, J. Mendez, Analysis of the different slip systems activated by tension in a α/β titanium alloy in relation with local crystallographic orientation, Acta Materialia. 53 (2005) 555–567. https://doi.org/10.1016/j.actamat.2004.09.040.

[54] On the mechanistic basis of deformation at the microscale in hexagonal close-packed metals | Proceedings of the Royal Society A: Mathematical, Physical and Engineering Sciences, (n.d.). https://royalsocietypublishing.org/doi/full/10.1098/rspa.2014.0881 (accessed February 10, 2021).

[55] Y. Zheng, R.E.A. Williams, G.B. Viswanathan, W.A.T. Clark, H.L. Fraser, Determination of the structure of α-β interfaces in metastable β-Ti alloys, Acta Materialia. 150 (2018) 25–39. https://doi.org/10.1016/j.actamat.2018.03.003.

[56] Titanium | Gerd Lütjering | Springer, (n.d.). https://www.springer.com/gp/book/9783540713975 (accessed September 10, 2020).

[57] C.L. Kelchner, S.J. Plimpton, J.C. Hamilton, Dislocation nucleation and defect structure during surface indentation, Phys. Rev. B. 58 (1998) 11085–11088. https://doi.org/10.1103/PhysRevB.58.11085.

[58] A.K. Ackerman, V.A. Vorontsov, I. Bantounas, Y. Zheng, T. McAuliffe, W.A. Clark, H.L. Fraser, D. Rugg, D. Dye, Interface characteristics in an {\alpha}+{\beta} titanium alloy, Phys. Rev. Materials. 4 (2020) 013602. https://doi.org/10.1103/PhysRevMaterials.4.013602.

[59] M. Kasemer, M.P. Echlin, J.C. Stinville, T.M. Pollock, P. Dawson, On slip initiation in equiaxed α/β Ti-6Al-4V, Acta Materialia. 136 (2017) 288–302. https://doi.org/10.1016/j.actamat.2017.06.059.

[60] Y. Chong, T. Bhattacharjee, M.-H. Park, A. Shibata, N. Tsuji, Factors determining room temperature mechanical properties of bimodal microstructures in Ti-6Al-4V alloy, Materials Science and Engineering: A. 730 (2018) 217–222. https://doi.org/10.1016/j.msea.2018.06.019.

[61] M.R. Bache, M. Cope, H.M. Davies, W.J. Evans, G. Harrison, Dwell sensitive fatigue in a near alpha titanium alloy at ambient temperature, International Journal of Fatigue. 19 (1997) 83–88. https://doi.org/10.1016/S0142-1123(97)00020-0.

[62] M. Risbet, X. Feaugas, C. Guillemer-Neel, M. Clavel, Use of atomic force microscopy to quantify slip irreversibility in a nickel-base superalloy, Scripta Materialia. 49 (2003) 533–538. https://doi.org/10.1016/S1359-6462(03)00357-9.

[63] Y. Liu, P. Samimi, I. Ghamarian, D.A. Brice, D.E. Huber, Z. Wang, V. Dixit, S. Koduri, H.L. Fraser, P.C. Collins, Discovery via Integration of Experimentation and Modeling: Three Examples for Titanium Alloys, JOM. 67 (2015) 164–178. https://doi.org/10.1007/s11837-014-1197-3.

[64] P.C. Collins, S. Koduri, V. Dixit, H.L. Fraser, Understanding the Interdependencies Between Composition, Microstructure, and Continuum Variables and Their Influence on the Fracture Toughness of α/β-Processed Ti-6Al-4V, Metall Mater Trans A. 49 (2018) 848–863. https://doi.org/10.1007/s11661-017-4443-9.

[65] P.O. Tympel, T.C. Lindley, E.A. Saunders, M. Dixon, D. Dye, Influence of complex LCF and dwell load regimes on fatigue of Ti–6Al–4V, Acta Materialia. 103 (2016) 77–88. https://doi.org/10.1016/j.actamat.2015.09.014.

[66] X. Wang, P. Vo, M. Jahazi, S. Yue, Dwell Fatigue Microstructure in a Near-α Titanium Alloy, Metall Mater Trans A. 38 (2007) 831–839. https://doi.org/10.1007/s11661-007-9105-x.

[67] M.N. Kelly, K. Glowinski, N.T. Nuhfer, G.S. Rohrer, The five parameter grain boundary character distribution of α-Ti determined from three-dimensional orientation data, Acta Materialia. 111 (2016) 22–30. https://doi.org/10.1016/j.actamat.2016.03.029.